AGU PUBLICATIONS

Global Biogeochemical Cycles

RESEARCH ARTICLE
10.1002/2014GB004814

Key Points:
- The first global 3-D ocean tracer model for mercury is developed
- Biological pump and water mass age mainly decide mercury distribution
- Comparison against present-day observations reveals human perturbation

Supporting Information:
- Figures S1–S4

Correspondence to:
L. Jaeglé,
jaegle@atmos.washington.edu

Citation:
Zhang, Y., L. Jaeglé, and L. A. Thompson (2014), Natural biogeochemical cycle of mercury in a global three-dimensional ocean tracer model, *Global Biogeochem. Cycles*, *28*, doi:10.1002/2014GB004814.

Received 24 JAN 2014
Accepted 21 APR 2014
Accepted article online 28 APR 2014

Natural biogeochemical cycle of mercury in a global three-dimensional ocean tracer model

Yanxu Zhang[1], Lyatt Jaeglé[1], and LuAnne Thompson[2]

[1]Department of Atmospheric Sciences, University of Washington, Seattle, Washington, USA, [2]School of Oceanography, University of Washington, Seattle, Washington, USA

Abstract We implement mercury (Hg) biogeochemistry in the offline global 3-D ocean tracer model (OFFTRAC) to investigate the natural Hg cycle, prior to any anthropogenic input. The simulation includes three Hg tracers: dissolved elemental (Hg^0_{aq}), dissolved divalent (Hg^{II}_{aq}), and particle-bound mercury (Hg^P_{aq}). Our Hg parameterization takes into account redox chemistry in ocean waters, air-sea exchange of Hg^0, scavenging of Hg^{II}_{aq} onto sinking particles, and resupply of Hg^{II}_{aq} at depth by remineralization of sinking particles. Atmospheric boundary conditions are provided by a global simulation of the natural atmospheric Hg cycle in the GEOS-Chem model. In the surface ocean, the OFFTRAC model predicts global mean concentrations of 0.16 p*M* for total Hg, partitioned as 80% Hg^{II}_{aq}, 14% Hg^0_{aq}, and 6% Hg^P_{aq}. Total Hg concentrations increase to 0.38 p*M* in the thermocline/intermediate waters (between the mixed layer and 1000 m depth) and 0.82 p*M* in deep waters (below 1000 m), reflecting removal of Hg from the surface to the subsurface ocean by particle sinking followed by remineralization at depth. Our model predicts that Hg concentrations in the deep North Pacific Ocean (>2000 m) are a factor of 2–3 higher than in the deep North Atlantic Ocean. This is the result of cumulative input of Hg from particle remineralization as deep waters transit from the North Atlantic to the North Pacific on their ~2000 year journey. The model is able to reproduce the relatively uniform concentrations of total Hg observed in the old deep waters of the North Pacific Ocean (observations: 1.2 ± 0.4 p*M*; model: 1.1 ± 0.04 p*M*) and Southern Ocean (observations: 1.1 ± 0.2 p*M*; model: 0.8 ± 0.02 p*M*). However, the modeled concentrations are factors of 5–6 too low compared to observed concentrations in the surface ocean and in the young water masses of the deep North Atlantic Ocean. This large underestimate for these regions implies a factor of 5–6 anthropogenic enhancement in Hg concentrations.

1. Introduction

The ocean plays a central role in the biogeochemical cycling of mercury (Hg). Sea-air exchange is a major source of Hg, accounting for ~1/3 of total emissions to the atmosphere [*Lamborg et al.*, 2002; *Mason et al.*, 2003; *Strode et al.*, 2007; *Sunderland and Mason*, 2007]. As a reservoir of Hg, the ocean is 50 times larger than the atmosphere [*Mason et al.*, 1994]. In the water, Hg undergoes methylation either in near-shore sediments or within the open ocean water column [*Hammerschmidt and Fitzgerald*, 2004; *Sunderland et al.*, 2009]. The resulting monomethylmercury (MMHg) is a neurotoxin, which can bioaccumulate in the food web [*Morel et al.*, 1998]. Consumption of marine fish represents one of the main pathways for human exposure to MMHg [*Mergler et al.*, 2007] and has been associated with adverse health effects such as deficits in neurocognitive function in adults and neurodevelopment delays in children [*Yokoo et al.*, 2003; *Cohen et al.*, 2005].

Anthropogenic influence on the Hg cycle is significant, with coal burning and metal mining having increased global atmospheric Hg deposition by factors of ~3–5 since 1850 as inferred from lake sediment and ice cores [*Fitzgerald et al.*, 2005; *Schuster et al.*, 2002; *Lamborg et al.*, 2002; *Fain et al.*, 2009]. There is also evidence for significant anthropogenic releases due to the use of Hg in precious metal mining prior to 1850 [*Cooke et al.*, 2009; *Elbaz-Poulichet et al.*, 2011]. Based on the all-time anthropogenic Hg inventory of *Streets et al.* [2011], *Amos et al.* [2013] estimate a factor of 7.5 increase in present-day Hg deposition compared to natural levels 3000 years ago, with most of the increase having occurred since 1450.

Within the ocean, Hg cycles among elemental (Hg^0_{aq}), divalent inorganic (Hg^{II}_{aq}), MMHg, dimethylmercury (DMHg), and particle-bound (Hg^P_{aq}) forms [*Mason and Fitzgerald*, 1993]. The dominant source of Hg to the ocean is atmospheric Hg^{II} deposition, with smaller contributions from rivers, benthic sediments, and hydrothermal vents [*Mason et al.*, 2012, and references therein]. Atmospheric wet and dry depositions supply

Hg^{II} to the surface ocean. In the mixed layer, Hg^{II}_{aq} can be reduced to Hg^{0}_{aq}, which is then reemitted to the atmosphere. Hg^{II}_{aq} can also be absorbed onto suspended organic-rich particulate matter to produce Hg^{P}_{aq} [*Mason et al*., 1995; *Amyot et al*., 1997; *Rolfhus and Fitzgerald*, 2001; *Fitzgerald et al*., 2007]. As part of the biological pump, Hg^{P}_{aq} sinks to the subsurface ocean. Remineralization of sinking particulate matter converts Hg^{P}_{aq} to Hg^{II}_{aq}, thus resupplying Hg in the dissolved pool at depth [*Strode et al*., 2010]. The hypoxic (low-oxygen) zone in the subsurface ocean is hypothesized to be an area of strong net biological methylation of Hg^{II}_{aq} to MMHg and/or DMHg [*Sunderland et al*., 2009; *Lehnherr et al*., 2011]. MMHg and DMHg are lost via biological and chemical demethylation to Hg^{II}_{aq} and Hg^{0}_{aq} [*Mason and Fitzgerald*, 1993; *Mason et al*., 1998; *Schaefer et al*., 2004]. Burial of Hg^{P}_{aq} in marine sediments is the terminal sink for Hg [*Lamborg et al*., 2002].

The shape of observed total Hg (Hg^{T}) profiles contains the signatures of these different processes. In the mixed layer, Hg^{T} concentrations can exhibit a maximum or minimum relative to subsurface waters depending on the relative roles of sources (atmospheric deposition and upwelling of Hg-rich waters) and sinks (evasion and scavenging onto particles). The thermocline/intermediate waters (between the bottom of the mixed layer down to 1000 m depth) often display a local maximum in Hg^{T}. This maximum has been interpreted as a Hg source from remineralization of sinking particulate matter, or as an anthropogenic signal from isopycnal transport of enriched surface waters from high-deposition regions, or as the signature of anthropogenic Hg penetration on sinking particulate matter [*Mason et al*., 1998; *Mason and Sullivan*, 1999; *Fitzgerald et al*., 2007; *Strode et al*., 2010]. In the deep ocean (>1000 m), Hg^{T} concentrations are relatively constant and sometimes slightly increase with depth [e.g., *Laurier et al*., 2004; *Lamborg et al*., 2012].

Measurements of Hg concentrations in the surface ocean with ultraclean trace metal techniques and improved analytical procedures started 30 years ago. While the global coverage of these measurements remains very sparse, it has been increasing in recent years, especially as a result of the ongoing GEOTRACES program (An International Study of Marine Biogeochemical Cycles of Trace Elements and Their Isotopes, http://www.geotraces.org). Open ocean surface concentrations of Hg^{T} are typically between 0.3 and 3 p*M* (picomolar, 1 p*M* = 10^{-12} mol L^{-1}), with most values in the 1–2 p*M* range [*Fitzgerald et al*., 2007; *Mason et al*., 2012, and references therein].

Measurements of Hg concentrations in deep ocean waters are even more limited and show values ranging from 0.7 p*M* to 2 p*M* [e.g., *Laurier et al*., 2004; *Mason et al*., 2001]. Some studies have suggested that higher concentrations in the high-latitude North Atlantic relative to the Southern Ocean and North Pacific reflect deep water scavenging of Hg as deep waters travel from the North Atlantic to the North Pacific [*Laurier et al*., 2004; *Fitzgerald et al*., 2007; *Cossa et al*., 2011]. In contrast, *Lamborg et al*. [2012] reported higher concentrations in the deep waters of the North Pacific compared to a station near Bermuda in the North Atlantic. They interpreted this as slow enrichment of deep waters when they receive input from remineralization of sinking particles. Further complicating the interpretation of these observed gradients are issues related to undersampling, natural variability, and especially analytical uncertainty, which can be on the order of 40% [*Fitzgerald et al*., 2007; *Lamborg et al*., 2012].

The marine Hg cycle has been investigated in several studies using box models representing the ocean with 3 to 14 boxes [*Mason et al*., 1994; *Lamborg et al*., 2002; *Mason and Sheu*, 2002; *Sunderland and Mason*, 2007; *Streets et al*., 2011; *Amos et al*., 2013]. While these simple models are a useful means to synthesize our current understanding of the Hg cycle, they cannot take into account the large regional variability in factors controlling marine Hg concentrations [*Fitzgerald et al*., 2007; *Mason et al*., 2012, and references therein]. Horizontal variability in atmospheric Hg^{II} deposition, mixed layer redox chemistry, air-sea exchange, vertical transport, and particle settling were taken into account by *Strode et al*. [2007] and *Soerensen et al*. [2010], who developed a two-dimensional slab ocean model interfaced with the GEOS-Chem atmospheric chemical transport model (http://geos-chem.org). However, this model did not include horizontal advection in the ocean and assumed fixed subsurface ocean concentrations of Hg. The important role of vertical advection/diffusion coupled with particle scavenging of Hg was further illustrated by *Strode et al*. [2010], who used a 1-D column box model with 50 vertical layers.

Here we present a new state-of-the-science three-dimensional offline ocean tracer model for Hg. This model builds on previous modeling efforts and is the first to couple marine Hg biogeochemistry with 3-D advection-diffusion in the global ocean. This new framework allows us to test mechanistic hypotheses about the Hg marine cycling via direct comparisons to observed profiles. In this paper, we conduct a 3-D simulation of the oceanic distribution of Hg under natural conditions, i.e., without concurrent or legacy anthropogenic Hg emissions

(pre-1450). The influence of anthropogenic Hg emissions is examined in a separate paper (Y. Zhang et al., Six centuries of changing oceanic mercury in a global 3-dimensional model, manuscript in preparation, 2014).

We first describe the physical tracer advection-diffusion model and our Hg biogeochemical scheme (section 2). In section 3, we discuss the modeled oceanic distribution of Hg and its speciation and relate this distribution to controlling processes. We then evaluate our model results against observations of Hg profiles in the deep ocean (section 4). Conclusions are summarized in section 5. The main questions we aim to address in this study are as follows: What was the global distribution of Hg in the oceans prior to any anthropogenic influence? What is the role of Hg scavenging by sinking particulates in controlling the vertical distribution of Hg? What factors control the speciation of Hg in the oceans? Can we explain observed differences in deep water Hg concentrations between the North Atlantic and North Pacific Oceans?

2. Model Description

We use the University of Washington three-dimensional offline ocean tracer model (OFFTRAC), which is driven by monthly physical ocean circulation archived from a general circulation model (section 2.1). Spatially distributed atmospheric Hg^0 concentrations and Hg^{II} deposition fluxes are obtained from a simulation of the natural Hg cycle in the GEOS-Chem chemical transport model (section 2.2). Our implementation of Hg biogeochemistry in OFFTRAC is described in section 2.3.

We initialize the OFFTRAC simulation with zero Hg concentrations in the oceans and impose climatological monthly physical transport fields, atmospheric Hg^0 concentrations, Hg^{II} deposition fluxes, and riverine inputs. OFFTRAC is then integrated for 10,000 years, until steady state is reached (i.e., repeating annual cycle in Hg concentrations at the surface and Hg concentrations in the deep ocean changing by less than 5% over 1000 years). The resulting budget is described in section 2.4.

2.1. Physical Ocean Tracer Model Description

The OFFTRAC model calculates advection and diffusion of tracers using monthly averaged along-isopycnal and cross-isopycnal mass fluxes from the Hallberg Isopycnal Model (HIM) [*Hallberg*, 1995; *Hallberg and Rhines*, 1996]. HIM uses a tripolar grid (with poles over Russia, Canada, and the South Pole) with 210 grid cells in the meridional coordinate (1/3° latitude resolution near the equator) and 360 cells in the zonal (1° longitude resolution). There are 49 vertical isopycnal layers referenced to 2000 db ranging from $\sigma_2 = 21.85$ to 37.90 kg m^{-3}. The model has two levels of Kraus-Turner-type mixed layer [*Kraus and Turner*, 1967] and two buffer layers allowing smooth entrainment/detrainment from/to underlying isopycnal surfaces.

As described in *Shao et al.* [2013], we run HIM for 650 years from an initially quiescent ocean with climatological mean isopycnal depths, temperature, and salinity. The model is forced at the surface by the normal year climatological Common Ocean Reference Experiment version 2 [*Large and Yeager*, 2009]. We use the monthly physical fields (monthly averages of mass transports, temperature, salinity, and monthly instantaneous snapshots of isopycnal thickness) averaged over the last 20 years of the 650 year HIM run to drive the OFFTRAC model.

Advection in the OFFTRAC model is calculated implicitly with 30 iterations with a 1 month time step. Transport due to unresolved eddies is parameterized by along-isopycnal diffusion [*Gent and Mcwilliams*, 1990] and cross-isopycnal diffusion as described in *Shao et al.* [2013]. Rapid air-sea exchange in the surface mixed layer is calculated using an Euler forward method with a 1 day time step. Calculated tracers include dissolved inorganic carbon, phosphorous, nitrate, CFC-11, CFC-12, oxygen, and SF_6. The OFFTRAC model has a diagnostic to calculate the age of a water mass, defined as the elapsed time since last contact with the atmosphere.

Previous applications of the OFFTRAC model include simulations of oxygen variability in the North Pacific Ocean [*Deutsch et al.*, 2005, 2006] and global Ocean [*Deutsch et al.*, 2011], transit time distributions and CFC-11 to infer ventilation rates in the North Atlantic and Southern Oceans [*Trossman et al.*, 2012], and mixed layer saturations of CFC-11, CFC-12, and SF_6 [*Shao et al.*, 2013].

2.2. Atmospheric Hg^{II} Deposition, Hg^0 Concentrations, and Riverine Fluxes From the GEOS-Chem Atmosphere-Ocean-Land Hg Simulation

The atmospheric boundary conditions for the OFFTRAC-Hg simulation are obtained from the GEOS-Chem Hg atmosphere-ocean-land simulation at 4° latitude by 5° longitude horizontal resolution. GEOS-Chem is a global three-dimensional atmospheric chemistry transport model driven by the GEOS-5 assimilated meteorological

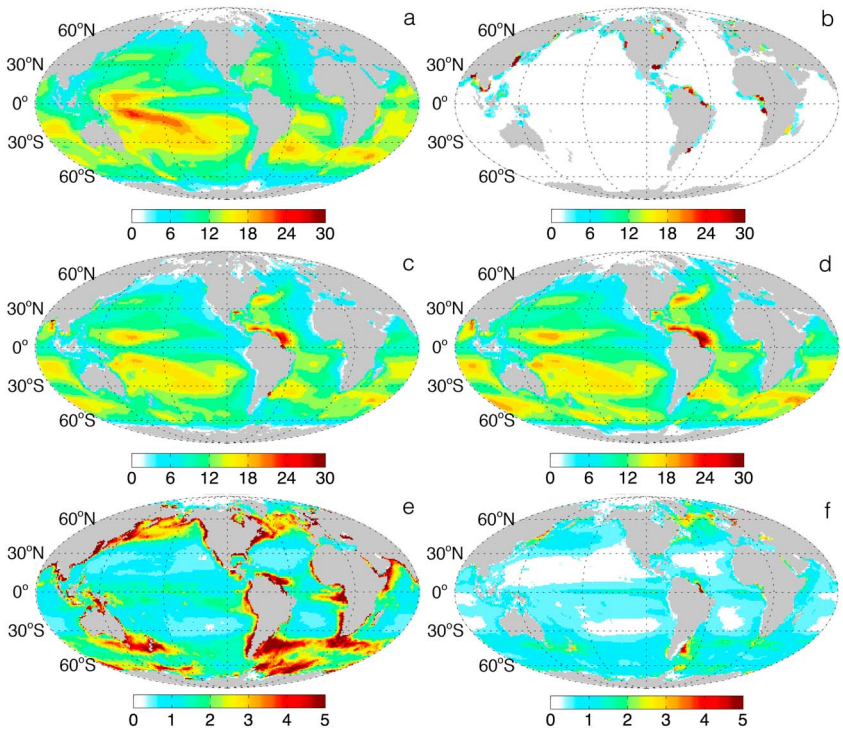

Figure 1. Annual mean fluxes (10^{-9} mol m^{-2} s^{-1}) for the natural OFFTRAC-Hg simulation: (a) atmospheric Hg^{II} deposition flux to the ocean, F_{dep}; (b) riverine Hg^{II}_{aq} input flux, $F_{riverine}$; (c) vertically integrated Hg^{II}_{aq} net reduction rate in the mixed layer; (d) Hg^{0} net evasion flux from the ocean to the atmosphere, $F_{evasion}$; (e) Hg^{P}_{aq} sinking flux at the bottom of mixed layer; and (f) Hg^{II}_{aq} net reduction rate vertically integrated below the mixed layer.

fields from the NASA Goddard Earth Observing System (GEOS). The GEOS-Chem Hg simulation (v9-01-02) is described in *Selin et al.* [2007] with updates from *Holmes et al.* [2010] and *Amos et al.* [2012]. This model includes three Hg tracers: elemental (Hg^0), divalent (Hg^{II}), and particulate-bound mercury (Hg^P). The model assumes that bromine atoms are the only oxidant for Hg^0 and that the reduction of Hg^{II} in cloud water is proportional to the photolysis rate of NO_2 [*Holmes et al.*, 2010]. The model also contains surface soil [*Selin et al.*, 2008] and slab ocean modules [*Strode et al.*, 2007; *Soerensen et al.*, 2010].

We conduct a natural GEOS-Chem Hg simulation in which we turn off all anthropogenic Hg sources. We assume that the only direct source of Hg is from a geogenic (i.e., volcanic) source of 0.45 Mmol a^{-1}, consistent with published estimates [*Mason and Sheu*, 2002; *Pirrone et al.*, 2010; *Bagnato et al.*, 2011]. This source is distributed according to the locations of Hg mines as an indicator of Hg deposits [*Selin et al.*, 2008, and references therein]. We use the results of the box model simulation of *Amos et al.* [2013] to impose global mean soil Hg concentrations (17 ng g^{-1}) and thermocline water Hg concentrations (0.28 p*M*) in GEOS-Chem. We spatially distribute soil Hg concentrations based on the balance between atmospheric deposition and soil reemission fluxes, while Hg concentrations in the subsurface water are assumed to be constant and uniformly distributed in GEOS-Chem.

We archive monthly GEOS-Chem atmospheric Hg^0 concentrations and Hg^{II} deposition fluxes to use as inputs to our OFFTRAC-Hg simulation. We calculate mean atmospheric boundary layer concentrations of Hg^0 of 0.20 ng/m^3 and a global Hg^{II} deposition flux to the ocean $F_{dep} = 3.9$ Mmol a^{-1}. While our estimate for F_{dep} is a factor of 2 lower relative to previous studies focusing on preindustrial time (circa 1850, e.g., 8.5 Mmol a^{-1} in *Selin et al.* [2008] and 6.8 Mmol a^{-1} in *Mason and Sheu* [2002]), it is consistent with more recent studies considering the legacy of precious metal mining activity prior to the industrial revolution [*Streets et al.*, 2011; *Amos et al.*, 2013].

The spatial distribution of F_{dep} largely follows both precipitation, which affects wet deposition, and wind speed, which controls removal of Hg by sea-salt particles (Figure 1a). Higher deposition fluxes in the Southern Hemisphere are due to faster atmospheric oxidation of Hg^0 caused by high Br atom concentrations (due to a larger oceanic source of bromocarbons) combined with faster deposition of Hg onto sea-salt particles [*Holmes et al.*, 2010].

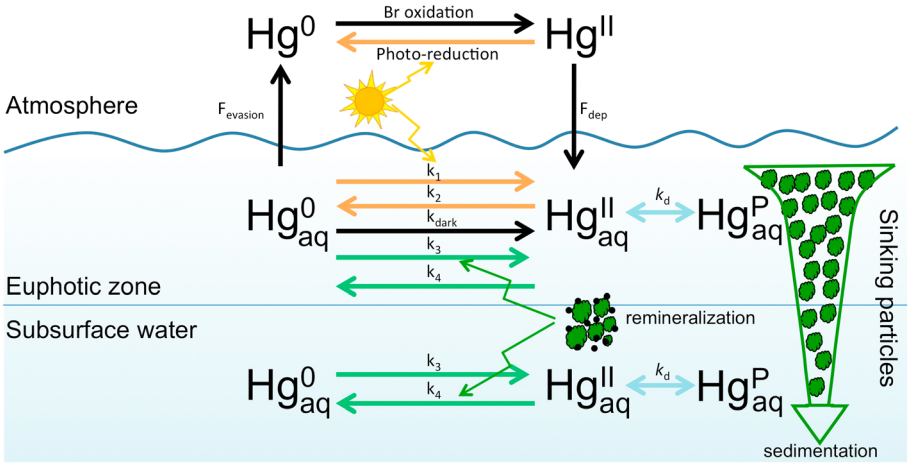

Figure 2. Schematic representation of Hg biogeochemistry in OFFTRAC-Hg. Coupling to the atmosphere includes deposition of Hg^{II} to the ocean (F_{dep}) and net evasion of Hg^0 ($F_{evasion}$). The orange arrows in the euphotic zone indicate photooxidation of Hg^0_{aq} to Hg^{II}_{aq} (k_1) and photoreduction of Hg^{II}_{aq} to Hg^0_{aq} (k_2), which are proportional to the short-wave radiation flux. Dark oxidation of Hg^0_{aq} (k_{dark}) is assumed to be constant. Biological oxidation and reduction rate constants (k_3 and k_4) are proportional to the local organic carbon remineralization rate (OCRR). Blue arrows represent the partitioning between Hg^{II}_{aq} and Hg^P_{aq} via sorption/desorption processes (k_d). Sinking particles transport Hg^P_{aq} downward with a flux proportional to the particulate organic carbon flux (F_{POC}).

We calculate the transport of Hg from land to ocean via rivers ($F_{riverine}$, $\times 10^3$ mol grid^{-1} s^{-1}) based on river runoff (R, $\times 10^6$ m^3 s^{-1}) and regional soil Hg concentrations (C_{soil}, ng g^{-1}), scaled by a constant ($k_{riverine}$, mol m^{-3} grid^{-1}):

$$F_{riverine} = k_{riverine} \cdot R \cdot C_{soil} \quad (1)$$

We use the climatological monthly mean freshwater discharge from continents developed by *Dai and Trenberth* [2002] with a spatial resolution of 1° × 1°. The values of C_{soil} are obtained by averaging the GEOS-Chem land model soil Hg concentrations in a 300 km radius surrounding individual river mouths. We tune the scaling constant ($k_{riverine} = 6.7 \times 10^{-1}$ mol m^{-3} grid^{-1}) to obtain a natural global riverine flux of 0.37 Mmol a^{-1}, following *Sunderland and Mason* [2007].

The predicted riverine Hg^{II} input flux is confined to coastal regions near river mouths (Figure 1b). The mouths of the largest rivers, including the Mississippi and Columbia Rivers in North America, Amazon and Orinoco Rivers in South America, Yangtze, Amur, Ob, and Yenisei Rivers in Asia, Congo, and Zambezi Rivers in Africa are identifiable in Figure 1b. The contribution of riverine input to Hg^T concentrations is shown in Figure S1 in the supporting information.

2.3. Hg Biogeochemistry in OFFTRAC

Our Hg simulation in OFFTRAC calculates the distribution of three Hg tracers: dissolved elemental Hg (Hg^0_{aq}), dissolved divalent Hg (Hg^{II}_{aq}), and particle-bound Hg (Hg^P_{aq}). For simplicity, we have chosen the Hg^{II}_{aq} tracer to represent all dissolved forms of inorganic and organic Hg complexes including MMHg and DMHg. As summarized in Figure 2 and Table 1, we consider the photochemical and biological redox conversion between Hg^0_{aq} and Hg^{II}_{aq} in the surface ocean, air-sea exchange of Hg^0, organic particle scavenging/remineralization processes in the water column, and subsurface reduction leading to Hg^0_{aq} production. Each of these processes is described below.

2.3.1. Surface Ocean Redox Reactions

In the ocean mixed layer, we model the photochemically and biologically mediated redox chemistry of Hg^{II}_{aq} and Hg^0_{aq} following the parameterization of *Strode et al.* [2007], with updates from *Soerensen et al.* [2010]. Briefly, the photochemical oxidation and photochemical reduction first-order rate constants (k_1 and k_2 in Figure 2 and Table 1) are proportional to short-wave radiation at the sea surface (RAD, from the GEOS-5 assimilated data) attenuated by dissolved organic carbon (DOC) [from *Hansell et al.*, 2009] and pigments in the surface ocean (C_{pig}, http://oceancolor.gsfc.nasa.gov). We implement biological oxidation and reduction processes as first-order rate constants (k_3 and k_4), which are proportional to the microbial remineralization of

Table 1. Description of the Main Processes and Input Fields Used in the OFFTRAC-Hg Simulation

Parameter	Description	Reference or Source
F_{dep}	Atmospheric wet and dry deposition flux of Hg^{II} to the ocean, mol m^{-2} s^{-1}	GEOS-Chem natural Hg simulation (section 2.2)
$F_{evasion}$	Net evasion flux of Hg^0 across the air-sea interface, mol m^{-2} s^{-1}	Section 2.3.2
$F_{riverine}$	Riverine input of Hg, $\times 10^3$ mol $grid^{-1}$ s^{-1}	*Sunderland and Mason* [2007]
$k_{riverine}$	Scaling constant for $F_{riverine}$, $k_{riverine} = 6.7 \times 10^{-1}$ mol m^{-3} $grid^{-1}$	Equation (1)
R	River runoff, $\times 10^6$ m^3 s^{-1}	*Dai and Trenberth* [2002]
C_{soil}	Soil Hg concentrations, ng g^{-1}	GEOS-Chem natural Hg simulation (section 2.2)
k_1	Photooxidation of Hg^0_{aq} to Hg^{II}_{aq}, s^{-1}, $k_1 = k_{photo\text{-}ox} \times RAD$, with $k_{photo\text{-}ox} = 6.6 \times 10^{-6}$ m^2 W^{-1} s^{-1}	*Soerensen et al.* [2010]
k_2	Photoreduction of Hg^{II}_{aq} to Hg^0_{aq}, s^{-1}, $k_2 = k_{photo\text{-}red} \times RAD$, with $k_{photo\text{-}red} = 1.6 \times 10^{-6}$ m^2 W^{-1} s^{-1}	*Soerensen et al.* [2010]
k_3	Biological oxidation of Hg^0_{aq} to Hg^{II}_{aq}, s^{-1}, $k_3 = k_{bio\text{-}ox} \times OCRR$, with $k_{bio\text{-}ox} = 140$ m^3 mol^{-1}	Equation (11)
k_4	Biological reduction of Hg^{II}_{aq} to Hg^0_{aq}, s^{-1}, $k_4 = k_{bio\text{-}red} \times OCRR$, with $k_{bio\text{-}red} = 86$ m^3 mol^{-1}	Equation (9)
k_{dark}	Dark oxidation of Hg^0_{aq} to Hg^{II}_{aq}, 1.0×10^{-7} s^{-1}	*Soerensen et al.* [2010]
k_d	Partition coefficient of Hg on to suspended particulate matter, $k_d = 2.1 \times 10^5$ L kg^{-1}	Section 2.3.3
f_{oc}	Fraction of suspended particulate matter as organic carbon, $f_{oc} = 0.1$	*Strode et al.* [2010]
$F_{POC}(z_0)$	Sinking flux of POC out of the euphotic zone, mol m^{-2} s^{-1}	Equation (6)
pe-ratio	Ratio of POC export to NPP out of the euphotic zone	*Dunne et al.* [2005]
z_0	Depth of euphotic zone, $z_0 = 75$ m	*Najjar and Orr* [1998]
b	Exponent for the decay of POC and F_{POC} with depth, $b = 0.9$	*Najjar and Orr* [1998]
POC	Particulate organic carbon concentration, kg L^{-1}	SeaWiFS in the mixed layer; equation (3) for subsurface
DOC	Dissolved organic carbon concentration, mg m^{-3}	*Hansell et al.* [2009]
C_{pig}	Pigment concentrations in the surface ocean, mg m^{-3}	http://oceancolor.gsfc.nasa.gov
OCRR	Organic carbon remineralization rate, mol m^{-3} s^{-1}	Equation (10)
T	Surface atmospheric temperature, °C	GEOS-5 assimilated data
Chl	Surface chlorophyll concentrations, mg m^{-3}	http://oceancolor.gsfc.nasa.gov
NPP	Net primary production, mol C m^{-2} s^{-1}	MODIS satellite data, http://oceancolor.gsfc.nasa.gov
RAD	Short-wave radiation flux, W m^{-2}	GEOS-5 assimilated data

particulate organic carbon as described in section 2.3.5. We also include a first-order reaction for the dark oxidation of Hg^0_{aq} in the mixed layer, k_{dark}. We assume that 40% of the Hg^{II}_{aq} is reducible to Hg^0_{aq}, following *Soerensen et al.* [2010].

In our modeling framework, these redox processes lead to a Hg^{II}_{aq} to Hg^0_{aq} global net reduction flux of 3.6 Mmol a^{-1} in the mixed layer (Figure 2). The spatial distribution of this reduction flux follows the distribution of Hg^{II} inputs from atmospheric deposition and rivers (Figure 1c). In particular, equatorial regions along the South American East Coast display very high reduction fluxes because of the large input from the Amazon River in Brazil and the Orinoco River in Venezuela (Figure 1b). Overall, the net reduction flux is larger near the equator because of its dependence on radiation.

2.3.2. Air-Sea Exchange

The bidirectional air-sea exchange of Hg^0 is calculated based on the concentration gradient across the air-sea interface normalized by Henry's law coefficient for Hg^0 [*Andersson et al.*, 2008] and the piston velocity using the parameterization of *Nightingale et al.* [2000], which is a function of wind speed and temperature (from the GEOS-5 meteorological fields). We include a temperature and salinity-corrected Hg^0_{aq} diffusivity [*Wilke and Chang*, 1955] and a temperature-corrected Schmidt number for CO_2 [*Poissant et al.*, 2000]. The result is calculated as the net exchange flux of Hg^0 of two competing gross fluxes in opposite directions.

We calculate a net Hg^0 evasion flux from the ocean to the atmosphere with a value $F_{evasion} = 3.9$ Mmol a^{-1}. The spatial distribution of this flux is controlled by the supersaturation of Hg^0 concentrations and wind speeds (Figure 1d). The net evasion flux is generally higher in the Southern Hemisphere, reflecting the higher atmospheric Hg^{II} deposition flux and the higher wind speeds. The larger evasion fluxes over the Southern Ocean are caused by strong upwelling of Hg-rich waters. The evasion is also large along the Gulf Stream due to the entrainment of subsurface Hg-rich waters.

2.3.3. Sorption of Hg^{II}_{aq} Onto Particles

Hg^{II}_{aq} species have a high affinity to suspended particles and are associated with organic ligands [*Fitzgerald et al.*, 2007]. Following *Morel et al.* [1998], we assume that there is reversible exchange between Hg^{II}_{aq} and Hg^{P}_{aq} and that the ratio of Hg^{P}_{aq} to Hg^{II}_{aq} is proportional to the local levels of particulate organic carbon (POC, kg L^{-1}):

$$\frac{Hg^{P}_{aq}}{Hg^{II}_{aq}} = \frac{k_d}{f_{oc}}\mathrm{POC} \tag{2}$$

where k_d is the partition coefficient in units of L/(kg of suspended particulate matter) and f_{oc} is the fraction of organic carbon in suspended particulate matter. We use $f_{oc} = 10\%$, following *Strode et al.* [2010]. At the ocean surface, we use the climatological monthly mean POC concentration derived from Sea-viewing Wide Field-of-view Sensor (SeaWiFS) ocean color (http://oceancolor.gsfc.nasa.gov). In subsurface waters, POC concentrations are calculated as a function of depth, z, based on a power law [*Lam et al.*, 2011; *Siddall et al.*, 2005]:

$$\mathrm{POC}(z) = \mathrm{POC}_0 \cdot \left(\frac{z}{z_0}\right)^{-b} \tag{3}$$

where POC_0 is the POC concentration at surface ocean from SeaWiFS. We assume $z_0 = 75$ m and $b = 0.9$ following the Ocean Carbon Model Intercomparison Project protocol [*Najjar and Orr*, 1998].

Measurements indicate that k_d ranges from 10^5 to 10^6 L kg^{-1} in estuarine and coastal waters [*Fitzgerald et al.*, 2007]. In sensitivity simulations, we varied k_d within this range and found that it influences deep ocean Hg concentrations via sinking and remineralization of particles (section 2.3.4). In our model, we choose $k_d = 2.1 \times 10^5$ L kg^{-1} in order to reproduce observed deep ocean Hg concentrations in the North Pacific Ocean and the natural Hg sedimentation flux, which should match the geogenic flux (0.45 Mmol a^{-1}) at steady state. We found that ±50% variations in k_d lead to ±10–20% variations in the amount of Hg^{P}_{aq} sinking into the deeper ocean calculated with our model.

2.3.4. Particle Sinking and Sedimentation

The sinking flux of Hg^{P}_{aq} as a function of depth is assumed to be proportional to the sinking flux of POC (F_{POC}, mol m^{-2} s^{-1}) and the Hg^{P}_{aq} to carbon ratio:

$$\frac{\partial}{\partial t} Hg^{P}_{aq}(z) = -\frac{\partial}{\partial z}\left(F_{POC}(z) \cdot \frac{Hg^{P}_{aq}(z)}{\mathrm{POC}(z)}\right) \tag{4}$$

with

$$F_{POC}(z) = F_{POC}(z_0) \cdot \left(\frac{z}{z_0}\right)^{-b} \tag{5}$$

We use the same z_0 and b values as in equation (3). The POC flux at the bottom of the euphotic layer, $F_{POC}(z_0)$, is based on the net primary production in the surface ocean (NPP, mol C m^{-2} s^{-1} derived from MODIS (Moderate Resolution Imaging Spectroradiometer) satellite data: http://oceancolor.gsfc.nasa.gov) and the ratio of POC export to NPP (the *pe-ratio* [*Dunne et al.*, 2005]):

$$F_{POC}(z_0) = \mathrm{NPP} \cdot \mathrm{pe} - \mathrm{ratio} \tag{6}$$

with

$$\begin{gathered} \text{pe-ratio} = -0.0081T + 0.0806\ln(\mathrm{Chl}) + 0.426 \\ 0.04 < \text{pe-ratio} < 0.72 \end{gathered} \tag{7}$$

where T is surface atmospheric temperature (°C) and Chl is the surface chlorophyll concentrations (mg Chl m^{-3}, http://oceancolor.gsfc.nasa.gov). By using equations (2), (3), (5), and (6), we obtain

$$\frac{\partial}{\partial t} Hg^{P}_{aq}(z) = -\frac{\partial}{\partial z}\left(\mathrm{NPP} \cdot \text{pe-ratio} \cdot \left(\frac{z}{z_0}\right)^{-b} \cdot \frac{k_d}{f_{oc}} \cdot Hg^{II}_{aq}(z)\right) \tag{8}$$

Globally, the Hg^{P}_{aq} sinking flux from the mixed layer is 0.72 Mmol a^{-1}. Its spatial distribution (Figure 1e) follows the distribution of $F_{POC}(z_0)$, which is elevated in Northern Hemisphere high-latitude oceans (due to enhanced nutrients input from terrestrial erosion) and over regions with strong upwelling (for example, at the equator, in the Southern Ocean, and along the west coasts of continents).

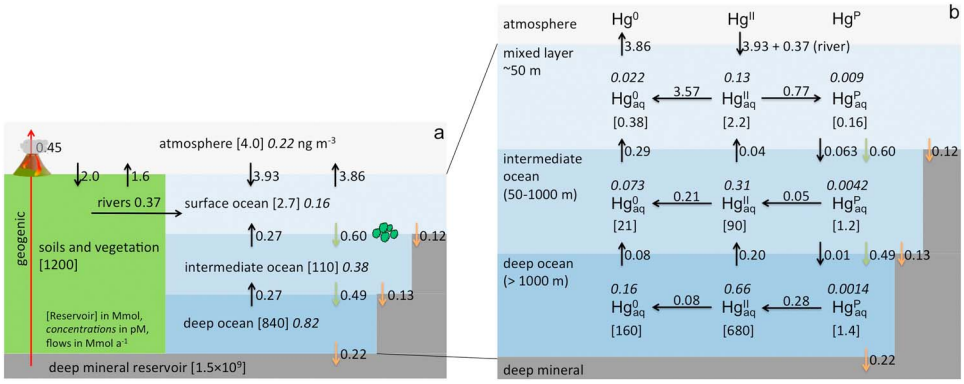

Figure 3. Global natural mercury budget in OFFTRAC-Hg: (a) global ocean-atmosphere-land system and (b) detailed ocean budget. The total Hg mass in each reservoir is indicated in brackets [units of Mmol], while concentrations are shown in italics (in p*M*, except for the atmosphere, where we use ng m^{-3}). Next to each arrow, the flux is indicated in Mmol a^{-1}. The geogenic source is shown as a red arrow, while the Hg particle sinking and sedimentation fluxes are shown as green and yellow arrows, respectively. The burdens of Hg in the deep mineral reservoir and soils are from *Andren and Nriagu* [1979] and *Amos et al.* [2013], respectively.

2.3.5. Subsurface Redox Reactions

Biologically mediated Hg redox reactions occur not only in the marine surface waters [*Rolfhus and Fitzgerald*, 2004; *Whalin et al.*, 2007] but also in deep waters without sunlight [*Mason et al.*, 1995; *Amyot et al.*, 1997; *Whalin et al.*, 2007]. These reactions are attributed to the activities of heterotrophic and chemotrophic microorganisms [*Mason et al.*, 1995; *Monperrus et al.*, 2007].

Based on observations of elevated concentrations of Hg^0_{aq} in the low-oxygen subthermocline region of the Equatorial Pacific Ocean, *Mason and Fitzgerald* [1993] hypothesized that ionic Hg^{II}_{aq} is converted into DMHg, which then decomposes via MMHg to Hg^0_{aq}. This mechanism was confirmed by observations in the Equatorial and South Atlantic Ocean [*Mason and Sullivan*, 1999] and in the Arctic Ocean [*Lehnherr et al.*, 2011]. *Sunderland et al.* [2009] found a positive linear relationship between MeHg concentrations and organic carbon remineralization rates (OCRR) in eastern North Pacific subsurface waters, providing evidence linking POC decomposition rates to bacterial methylation processes. Therefore, we scale the biologically mediated reduction of Hg^{II}_{aq} to Hg^0_{aq} (k_4, s^{-1}) to OCRR, which is a measure of the microorganism activity:

$$k_4 = k_{\text{bio-red}} \cdot \text{OCRR}(z) \tag{9}$$

where $k_{\text{bio-red}}$ is a constant and OCRR (mol m^{-3} s^{-1}) is calculated as the remaining fraction of NPP after export in the euphotic layer and as the vertical gradient of F_{POC} in subsurface waters:

$$\text{OCRR}(z) = \begin{cases} \dfrac{\text{NPP}}{z_0} \cdot (1 - \text{pe-ratio}) & z < z_0 \\ -\dfrac{\partial}{\partial z} F_{\text{POC}}(z) & z > z_0 \end{cases} \tag{10}$$

Similar to the surface waters, we assume that 40% of the Hg^{II}_{aq} is reducible to Hg^0_{aq} in the subsurface waters.

We also consider biologically mediated oxidation of Hg^0_{aq} [*Poulain et al.*, 2007], which we parameterize as a first-order rate constant proportional to OCRR:

$$k_3 = k_{\text{bio-ox}} \cdot \text{OCRR}(z) \tag{11}$$

Note that we ignore the dark oxidation of Hg^0_{aq} to Hg^{II}_{aq} in subsurface waters, as it requires prior exposure to sunlight [*Amyot et al.*, 1997]. We chose the values for $k_{\text{bio-ox}}$ (140 m^3 mol^{-1}) and $k_{\text{bio-red}}$ (86 m^3 mol^{-1}) so as to best reproduce observed profiles of Hg^0_{aq} concentration and the Hg^0_{aq} net evasion flux.

The vertically integrated net reduction rate (Figure 1f) is elevated over high POC export regions in the productive regions of the high-latitude oceans and equatorial upwelling regions. Overall, we obtain a global net reduction rate of 0.21 Mmol a^{-1} in thermocline/intermediate waters (Figure 3), with a gross reduction rate

of 3.34 Mmol a^{-1} and gross oxidation of 3.13 Mmol a^{-1}. In deep waters, the net reduction rate is 0.08 Mmol a^{-1} (0.88 Mmol a^{-1} gross reduction and 0.80 Mmol a^{-1} gross oxidation). The corresponding mean net reduction rate constants are 6.4×10^{-6} d^{-1} in thermocline/intermediate waters and 3.2×10^{-7} d^{-1} in deep waters. For comparison, *Lehnherr et al.* [2011] measured values ranging from below detection to 2.6×10^{-5} d^{-1} in the subsurface oxycline waters of the Arctic Ocean.

In a sensitivity simulation, we turned off Hg redox reactions in subsurface waters (i.e., by setting k_3 and k_4 to zero). This leads to very low Hg^0_{aq} concentrations (< 0.01 p*M*) in the subsurface ocean, indicating that a subsurface source for Hg^0_{aq} is necessary to maintain Hg^0_{aq} concentrations at levels that are consistent with observations [*Mason et al.*, 1998; *Mason and Sullivan*, 1999; *Cossa et al.*, 2011].

2.4. Global Hg Budget

The global Hg budget under natural conditions as simulated in OFFTRAC-Hg assumes that the atmosphere receives emissions from a direct geogenic source (0.45 Mmol a^{-1}) as well as reemissions from land (1.6 Mmol a^{-1}) and the ocean (3.86 Mmol a^{-1}) (Figure 3a). These inputs are balanced by the loss of Hg to land and ocean surfaces. The surface ocean (the depth varies spatially and seasonally, with a global average depth of ~50 m) receives 3.93 Mmol a^{-1} from atmospheric Hg^{II} deposition, 0.37 Mmol a^{-1} from rivers, and 0.27 Mmol a^{-1} from advection from the thermocline. We find that 82% of the mixed layer Hg is lost by net evasion to the atmosphere as Hg^0, with the remaining 18% by sinking to the thermocline on particles or by sedimentation in coastal and near-shelf sediments.

In the thermocline/intermediate waters, the main source of Hg is via particle sinking from the surface ocean (0.60 Mmol a^{-1}), with a smaller contribution from upward advection of deep ocean Hg (0.27 Mmol a^{-1}). This is consistent with previous models [*Strode et al.*, 2010; *Mason et al.*, 2012; *Amos et al.*, 2013]. We find that 70% of the Hg in the thermocline/intermediate waters is lost via downward particle sinking and 30% via upward transport to the mixed layer (Figure 3). In our model, the source of Hg to the deep ocean is via particle sinking (0.49 Mmol a^{-1}), which is subsequently deposited to sediments (0.22 Mmol a^{-1}) or transported back to the thermocline/intermediate water (0.27 Mmol a^{-1}).

The predicted residence times of Hg in the deep ocean (1700 years) and thermocline/intermediate water (120 years) are much longer than in the surface ocean (7 months) and atmosphere (8 months). We find an overall lifetime of Hg in the ocean against sedimentation of 2000 years, similar to the ocean's overturning time scale [*Schmittner et al.*, 2007]. Our overall Hg lifetime is close to the ~3000 years found by *Mason and Sheu* [2002]. This agreement is the result of similar assumptions for geogenic emission flux and total oceanic Hg mass. Our estimate is longer than the 600 years found by *Selin et al.* [2008], who assumed higher geogenic emissions (2.5 Mmol a^{-1}) and thus a higher oceanic sedimentation flux. We also find a longer residence time compared to the 1400 years estimated by *Amos et al.* [2013], even though we assume the same geogenic source. This discrepancy is likely caused by their representation of the ocean as three boxes, which assumes full mixing in the thermocline and deep water. This assumption leads to an overestimate of the vertical transport [*Siegenthaler and Oeschger*, 1978], thus lowering the oceanic Hg burden and overall residence time.

3. Modeled Oceanic Distribution of Hg

The modeled distribution of Hg in our natural ocean simulation is presented in maps of Hg^T concentrations at the surface, 1000 m and 3000 m (Figure 4) and in meridional cross sections through the Pacific and Atlantic Oceans (Figure 5). We discuss these figures below.

3.1. Surface Concentrations

At the surface, we calculate a global mean Hg^T concentration of 0.16 p*M* in the natural ocean (Figure 4a). Open ocean Hg^T concentrations are fairly uniform, and their pattern reflects the balance between local inputs (atmospheric deposition and upwelling) and removal (particulate sinking and evasion). For example, in the western Equatorial Pacific Ocean, Hg^T reaches 0.25 p*M*, because of strong atmospheric deposition combined with weak scavenging from particulate sinking (Figures 1a and 1e). Along the circumpolar Antarctic current, upwelling of Hg-rich waters results in high modeled surface concentrations, exceeding 0.5 p*M*. The suppressed evasion because of Antarctic sea ice also helps to build up high concentrations (Figure 1d). Some of the highest Hg^T concentrations are modeled along coastal areas as a

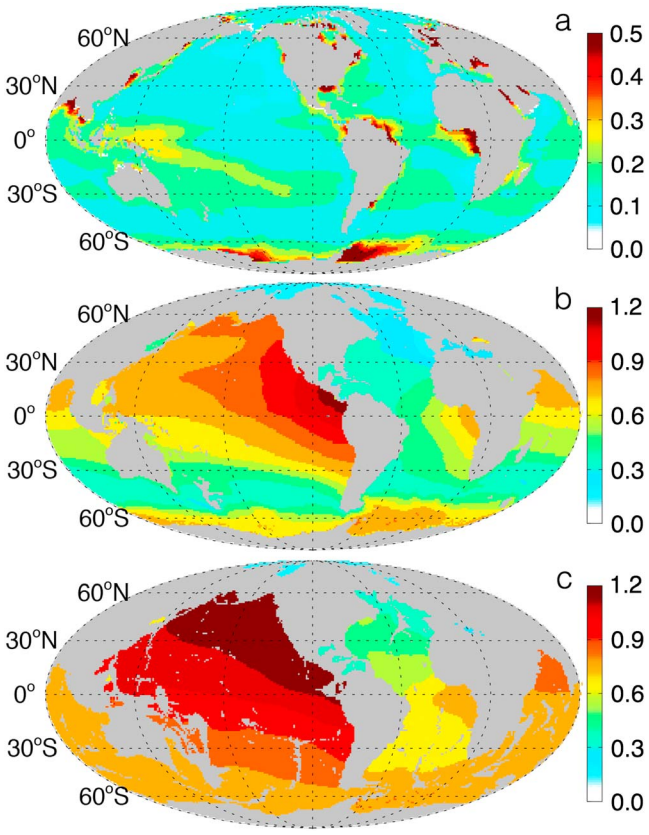

Figure 4. Annual mean concentrations of Hg^T (p*M*): (a) mixed layer, (b) 1000 m depth, and (c) 3000 m depth. Note the different color scale in Figure 4a.

result of riverine Hg input (Figures 1b and S4). In particular, closed and shallow water bodies such as Hudson Bay and the Black Sea display elevated Hg concentrations (> 1 p*M*).

In the present-day ocean, surface observations of Hg^T are highly variable, with mean values of 1.0 ± 1.5 p*M* as summarized in *Strode et al.* [2007] and *Soerensen et al.* [2010]. Our calculated natural ocean concentrations are thus a factor of 6 lower than these observations, with the difference reflecting anthropogenic influence.

Our model predicts that 80% of Hg in the surface ocean is in the form of Hg^{II}_{aq} (mean global concentrations of 0.13 p*M*), with much smaller contributions from Hg^0_{aq} and Hg^P_{aq} (14% and 6%, respectively). The modeled surface concentrations of Hg^0_{aq} range from 10 to 50 f*M* (femtomolar, 1 f*M* = 10^{-15} mol L^{-1}), accounting for 10 to 20% of Hg^T. This is consistent with observations reporting that Hg^0 accounts for 2–15% of Hg^T in the Equatorial Pacific Ocean [*Mason and Fitzgerald*, 1993] and 10–22% of Hg^T in the west Atlantic Ocean [*Soerensen et al.*, 2013]. However, other studies suggest a much larger Hg^0_{aq} fraction (20–40%) in surface waters of the Atlantic Ocean [*Mason and Sullivan*, 1999; *Mason et al.*, 1998]. In these studies, the authors suggest that these high values might reflect a net accumulation of Hg^0_{aq} over the summer from reduction of Hg^{II}_{aq}, and thus might not representative of annual average concentrations.

The model predicts that ~80% of Hg^{II}_{aq} is reduced to Hg^0_{aq} in the mixed layer, with the rest being partitioned onto particles (Figure 3b). In addition to production of Hg^0_{aq} by net reduction of Hg^{II}_{aq}, upward transport from intermediate waters (0.29 Mmol a^{-1}) is another source of Hg^0_{aq}. The supersaturation of Hg^0_{aq} results in rapid evasion to the atmosphere, leading to a 1 month mean residence time of Hg^0_{aq} in the surface ocean.

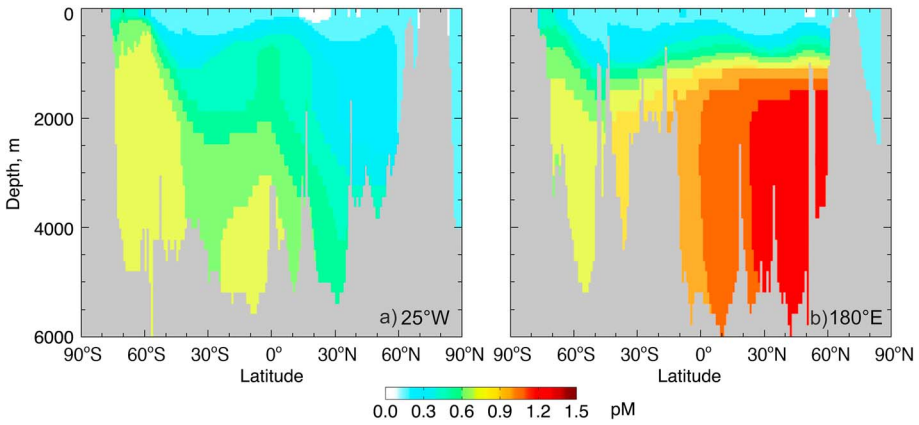

Figure 5. Cross sections of annual mean Hg^T concentrations: (a) Atlantic Ocean at 25°W and (b) Pacific Ocean at 180°E.

3.2. Subsurface Water Concentrations

Hg^T concentrations increase with depth, with mean concentrations of 0.38 p*M* in the thermocline/intermediate water and 0.82 p*M* in the deep ocean (Figures 3a, 4b, and 4c). At the surface, adsorption of Hg onto sinking particles represents a net removal of Hg. However, in subsurface waters particles become a source of Hg, as both the net desorption of Hg from particles and the decomposition of the sinking particles release Hg^{II}_{aq} (0.33 Mmol a^{-1}) (Figure 3b). Thus, Hg is transported as Hg^{P}_{aq} via particle sinking from the mixed layer to the deeper ocean, where it is remineralized to Hg^{II}_{aq} and then reduced to Hg^{0}_{aq}. Hg^{0}_{aq} then cycles back to surface waters via ocean advection and diffusion (Figure 3b). This cycling mediated by particles leads to the net increase of Hg^T with depth in our simulation.

At 1000 m and 3000 m depths, the model predicts large interbasin differences for Hg^T concentrations. At 3000 m depth (Figure 4c), the lowest concentrations are calculated in the North Atlantic Ocean (0.4–0.5 p*M*) and South Atlantic Ocean (0.6–0.8 p*M*). The Southern Ocean and Indian Ocean display higher concentrations (0.7–0.9 p*M*). The model predicts the highest Hg^T concentrations in the North Pacific Ocean (1.0–1.3 p*M*). Thus, our model predicts a progressive increase of Hg^T concentrations with water age (see map of water age in the supporting information, Figures S2 and S3). The younger water masses of the North Atlantic Ocean (water mass age of 1200 years) keep the signature of low surface Hg^T concentrations, while the older waters in the deep Indian Ocean (1900 years) and North Pacific Ocean (>2000 years) have received continuous input of Hg from degradation of organic material during their transport along the thermohaline circulation. This leads to a factor of 2–3 increase in Hg^T concentrations between the deep North Atlantic and deep North Pacific.

Modeled Hg^T concentrations at 1000 m depth (Figure 4b) display much of the same pattern as at 3000 m, with a factor of 2–3 increase in Hg^T between the North Atlantic Ocean (0.2–0.4 p*M*) and the North Pacific Ocean (0.7–0.9 p*M*). The highest Hg^T concentrations at 1000 m depth are predicted in the eastern Equatorial Pacific Ocean (0.9–1.2 p*M*, Figure 4b), rather than the North Pacific Ocean as at 3000 m depth (Figure 4c). This maximum in the eastern Equatorial Pacific is caused by the strong input from particle sinking (Figure 1e) combined with input from upwelling of Hg-rich deep waters. In the circumpolar Antarctic current, upwelling also leads to higher total Hg concentrations relative to the Southern Ocean (Figure 4b).

A cross section in the Atlantic Ocean at 25°W (Figure 5a) illustrates the influence of deep water formation in the high-latitude North Atlantic, where low Hg^T concentrations (0.2–0.4 p*M*) extend from the surface ocean to 3000 m depth. Concentrations in the deep ocean increase from north to south in the Atlantic Ocean and from south to north in the Pacific Ocean (180°E, Figure 5b) following the increasing water age along the abyssal thermohaline circulation. In intermediate waters near 1000 m, the contours of Hg^T generally follow density contours, reflecting the importance of stratification and isopycnal transport [*Brown et al*., 2002]. Hg-rich water in the deep ocean upwells to the base of the thermocline and forms bulges of high Hg concentrations over equatorial regions and in the Southern Ocean, where the thermocline rises toward the surface. Conversely, downwelling over the centers of the gyres at 30°–40° latitude causes lower total Hg concentrations in thermocline/intermediate waters at the same depth.

Our prediction of a progressive increase in Hg^T concentrations as deep water travels from the North Atlantic to the North Pacific is similar to the behavior of biologically active tracers (nitrate, phosphate, silicate, and CO_2) and some trace metals (cadmium, nickel, zinc, and silver), which display higher concentrations in deep Pacific Ocean waters relative to the deep North Atlantic Ocean waters [*Bruland and Lohan*, 2004; *Emerson and Hedges*, 2008]. Indeed, observed profiles of cadmium and zinc show a factor of 4–6 enrichment at 1000 m depth in the North Pacific Ocean compared to the North Atlantic [*Aparicio-González et al*., 2012], similar to the enrichment we find for Hg. In contrast, aluminum and iron, with large aeolian input in the North Atlantic, have the opposite trend indicating scavenging during transit [*Boyd and Ellwood*, 2010].

As deep water accumulates metabolic residue from degradation of organic material, dissolved oxygen is being consumed. Our simulation thus predicts that the spatial distribution of Hg at intermediate depths is anticorrelated with the distribution of dissolved oxygen (see maps of oxygen concentrations in the supporting information, Figure S4). For example, the eastern tropical Pacific Ocean and northern Indian Ocean display the lowest levels of dissolved O_2 because of the strong particle sinking flux and respiration [*Deutsch et al*., 2011].

Table 2. Summary of Cruises With Deep Ocean Total Hg Concentration Measurements

Cruise/Station[a]	Region	Date	Hg^T Concentrations, p*M* (> 2000 m)[b] Obs.	Model	Reference
		North Pacific Ocean			
IOC 2002 (a–c)	NW Pacific (20°–50°N 120°E–160°W)	May–Jun 2002	1.2 ± 0.3	1.1 ± 0.03	*Laurier et al.* [2004]
VERTEX (d)	NE Pacific (25°N–60°N, 130°–150°W)	Jul–Aug 1987	1.0 ± 0.2	1.2 ± 0.04	*Laurier et al.* [2004]
SAFe (e)	NE Pacific (30°N, 140°W)	May 2009	1.4 ± 0.2	1.1 ± 0.04	*Hammerschmidt and Bowman* [2012]
		Southern Ocean			
SR3 CASO-GEOTRACES (f–i)	Antarctica/Tasmania (44°–66°S, 140°–147°E)	Mar–Apr 2008	1.1 ± 0.2	0.8 ± 0.02	*Cossa et al.* [2011]
		South and Equatorial Atlantic Ocean			
Dutch South Atlantic Expedition (j–l)	(50°S–0°S, 28°W–53°W)	Mar 2011	0.6 ± 0.2	0.7 ± 0.05	*Bowman et al.* [2012]
		North Atlantic Ocean			
BATS (m)	31°N, 64°W	Mar 2000	0.7 ± 0.3	0.5 ± 0.06	*Mason et al.* [2001]
BATS (m)	31°N, 64°W	Jun 2008	1.1 ± 0.05	0.5 ± 0.06	*Lamborg et al.* [2012]
OMEX (n and o)	Edge of Celtic Sea (47°N–50°N, 6°W–14°W)	Jan 1994 Jun 1995	2.2 ± 0.5	0.4 ± 0.08	*Cossa et al.* [2004]
IOC 1993 (p and q)	Subarctic North Atlantic (47°N–68°N, 60°W–0°W)	Aug 1993	1.7 ± 0.4	0.3 ± 0.04	*Mason et al.* [1998]
US North Atlantic Expedition 2011 Leg (r–v)	North Atlantic (15°N–40°N, 10°W–70°W)	Nov–Dec 2011	1.1 ± 0.2	0.5 ± 0.07	(K. L. Bowman et al., in review, 2014)

[a]Each profile is given a letter code between a and w, with its location indicated in Figure 6.
[b]Total Hg concentrations at depths below 2000 m (in p*M*). The mean and standard deviation of observed and modeled values are indicated in separate columns.

4. Profiles of Hg in Different Ocean Basins

In order to evaluate our simulation, we examine vertical profiles of Hg concentrations from 10 individual studies (Table 2 and Figure 6). Hg concentrations in surface, thermocline, and intermediate waters are believed to have been perturbed by anthropogenic activities [*Mason et al.*, 1994; *Strode et al.*, 2010]; we thus focus our comparison on profiles extending below 2000 m where the concentrations are more likely to reflect preanthropogenic conditions. For this comparison, we sample the model at the location of the observed profiles. Because the topography is smoothed in the model, the depth in the modeled profile may be different from the depth in the real ocean.

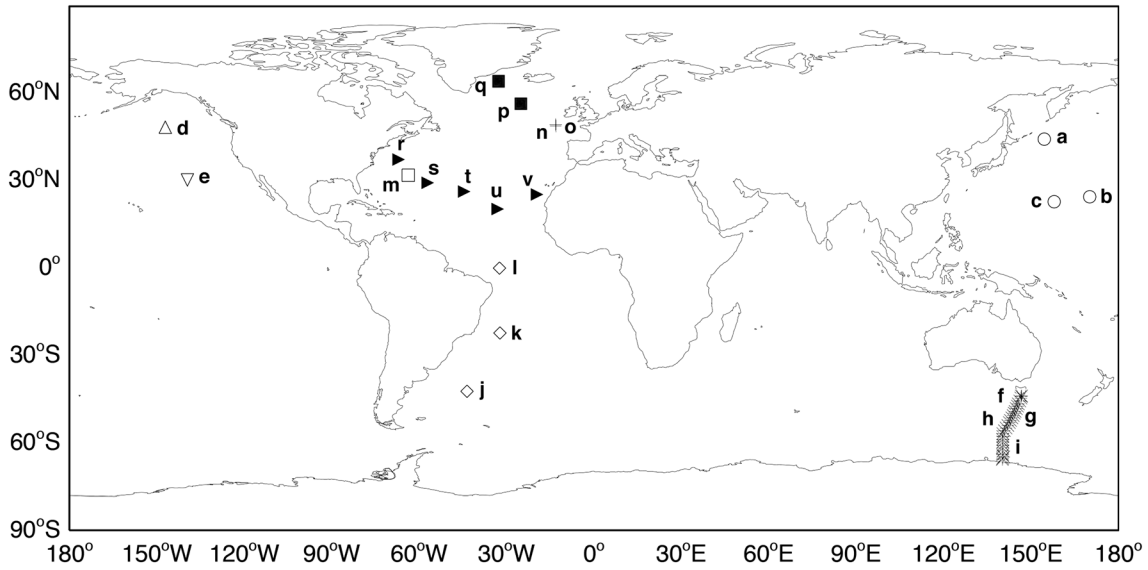

Figure 6. Location of observed profiles used for evaluating the OFFTRAC natural Hg simulation. Circle, 2002 IOC (profiles a–c); triangle, VERTEX (profile d); inverted triangle, SAFe (profile e); cross, SR3 CASO-GEOTRACES (profiles f–i); diamond, Dutch South Atlantic Expedition (profiles j–l); square, BATS (profile m); plus, OMEX 1994–1995 (profiles n and o); filled square, 1993 IOC (profiles p and q); and filled right-pointing triangle US North Atlantic Expedition 2011 Leg (profiles r–v). See Table 2 for more details.

4.1. Comparisons to Observed Profiles

Observed deep water concentrations of Hg^T in the North Pacific Ocean are relatively homogeneous [*Laurier et al.*, 2004; *Hammerschmidt and Bowman*, 2012], with mean values of 1.0–1.4 p*M* (Table 2 and Figures 7a–7e). Our modeled deep water concentrations of 1.1–1.2 p*M* in the North Pacific Ocean agree well with observed profiles and display fairly constant Hg^T concentrations below 2000 m, similar to observations (Figures 7a–7e).

Profiles collected in the Southern Ocean along a transect between Antarctica and Tasmania [*Cossa et al.*, 2011] display Hg^T concentrations of 1.1–1.4 p*M* (Table 2 and Figures 7f–7i). In the deep ocean between 45°S and 52°S, model (~0.8 p*M*) and observations (~1.0 p*M*) have similar Hg^T concentrations (Figure 7f). Poleward of 52°S (Figures 7g–7i), elevated concentrations are observed in the surface and in deep waters, which *Cossa et al.* [2011] attributed to net atmospheric Hg^{II} deposition input near the ice edge and subsequent downward transfer during deep water formation in winter months. These high observed concentrations contain a signature from the anthropogenic emissions, which are not included in our model simulation of the natural Hg cycle. For these regions, the model is a factor of 2 lower than observations.

In deep waters of the Equatorial and South Atlantic Ocean, *Bowman et al.* [2012] report Hg^T concentrations of 0.5–0.7 p*M* (Figure 7j–7l). The model predicts 0.7 p*M* in this region. Higher Hg^T concentrations up to 1 p*M* are measured near the ocean floor (Figure 7j), reflecting Hg input from a local hydrothermal vent. *Mason and Sullivan* [1999] measured high Hg concentrations up to 10 p*M* near the ocean floor in this region in 1996. However, the influence of hydrothermal vents, which we do not include in our model simulation, is expected to be limited to regions near the vents [*Lamborg et al.*, 2006].

Midlatitude North Atlantic waters near the Bermuda Atlantic Time-series Study (BATS) station show deep ocean concentrations ranging from 0.7 p*M* to 1.2 p*M* (Figure 7m) [*Mason et al.*, 2001; *Lamborg et al.*, 2012]. Our modeled concentrations (0.5 p*M*) are slightly lower than the 0.7 ± 0.3 p*M* concentrations measured by *Mason et al.* [2001], but a factor of 2 lower than the values reported by *Lamborg et al.* [2012] at the same site (Figure 7m). Similarly, the model is a factor of 2 lower than the North Atlantic profiles obtained by K. L. Bowman, et al. (Mercury in the North Atlantic Ocean: The U.S. GEOTRACES zonal and meridional transects, in review, *Deep Sea Research II*, 2014) (Figures 7r–7v). At higher latitudes over the Atlantic Ocean, *Cossa et al.* [2004] (Figures 7n–7o) and *Mason et al.* [1998] (Figures 7p and 7q) measured high Hg^T concentrations of 1.7–2.2 p*M* below 2000 m (Table 2). The modeled concentrations are 0.3–0.4 p*M*, a factor of 5–6 lower than observations. As discussed by *Mason et al.* [1998], deep water formation is occurring in the subarctic North Atlantic Ocean (e.g., Figure 7q). The difference between model and observations over this region could thus be the result of deep ocean penetration of anthropogenic Hg influence from both atmospheric input and riverine effluent. It is also possible that the model lacks important processes that control North Atlantic intermediate deep water formation. As for the observations at the shelf edge of the Celtic Sea, on the western European continental margin by *Cossa et al.* [2004] (Figures 7n and 7o), the observed high Hg^T concentrations may also carry strong anthropogenic signals from riverine input and/or direct industrial/waste water discharge.

In summary, our modeled Hg^T concentrations in the natural ocean are within 50% of observations in old and deep water masses of the North Pacific Ocean, the Southern Ocean, South Atlantic Ocean, and midlatitude North Atlantic Ocean. Considering the interlaboratory comparability of Hg measurements (on the order of 40% [*Lamborg et al.*, 2012]) this level of agreement is within analytical uncertainty. We find that the model significantly underpredicts observed Hg^T concentrations for younger water masses in deep water formation regions of the Southern Ocean and North Atlantic, which contain a strong signature from the human perturbation. The difference between our natural Hg cycle concentrations and observations in these regions can be used to generate a first-order estimate of the anthropogenic influence: factors of 5–6 enhancement in deep water formation regions of the North Atlantic (which is consistent with our factor of 6 underestimate of present-day surface observations) and factor of 2 for the Northern midlatitude Atlantic Ocean and high-latitude Southern Ocean.

4.2. Interocean Fractionation

In past studies, interocean comparisons of observed deep water Hg concentrations have yielded contradictory interpretations. Studies based on contrasting higher concentrations in the Atlantic (found at high northern latitudes, equatorial, and tropical waters) to the lower concentrations in the North Pacific, were interpreted as resulting from deep water scavenging of Hg as deep waters travel from the North Atlantic to the North Pacific [*Laurier et al.*, 2004; *Fitzgerald et al.*, 2007]. Similarly, *Cossa et al.* [2011] suggested that the lower concentrations

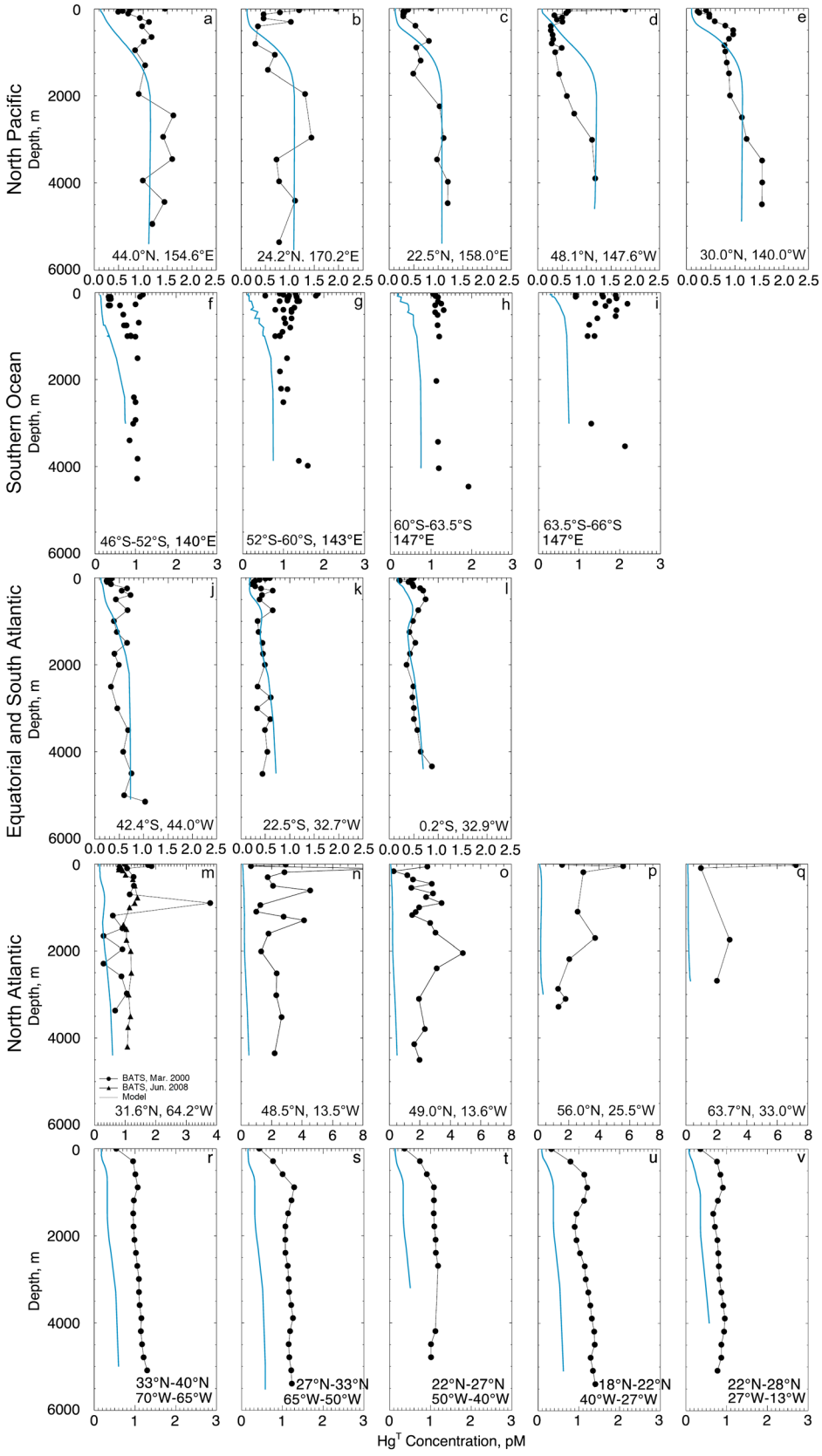

Figure 7. Comparison between observed (black circles and lines) and modeled (blue lines) oceanic Hg^T concentration profiles. (a–v) The location for each profile is indicated in Figure 6.

measured in the Southern Ocean compared to the North Atlantic Deep Waters reflected particle removal during transit. In contrast, *Lamborg et al*. [2012] found higher concentrations in the deep waters of the NE Pacific than at the BATS station in the North Atlantic, which they interpreted as resulting from slow Hg enrichment of deep waters receiving input from remineralization of sinking particles.

Our modeling study supports the interpretation proposed by *Lamborg et al*. [2012]. We find a factor of 2–3 enrichment in Hg between deep waters of the North Atlantic and of the North Pacific in the natural ocean. As noted in section 3.2, this enrichment is similar to that observed for zinc and cadmium, which are not perturbed by human activities. For Hg, it appears that penetration of anthropogenic emissions in regions influenced by deep water formation in the North Atlantic has increased Hg concentrations, thus dampening the interbasin gradient. The continuous input from remineralization from sinking particles as the water ages in transit from source regions in the North Atlantic to the North Pacific is thus overprinted with a large anthropogenic signal.

5. Conclusions

We have implemented Hg biogeochemistry in a state-of-the-science 3-D offline ocean tracer model, OFFTRAC-Hg. While our oceanic model represents Hg biochemistry in a simplified way, it allows us to examine current knowledge of marine Hg cycling and it creates a useful framework to test mechanistic hypotheses about this complex system via comparisons to observed oceanic profiles.

We conducted a simulation of the natural cycle of Hg in the ocean-atmosphere-land system by coupling OFFTRAC to the GEOS-Chem atmosphere-land-ocean model. In our simulation, the only direct source of Hg is a geogenic source of 0.45 Mmol a^{-1}. Of the resulting 3.93 Mmol a^{-1} atmospheric deposition and 0.37 Mmol a^{-1} riverine input in the form of Hg^{II}_{aq} in the mixed layer, 82% is reduced to Hg^{0}_{aq} and evaded back to the atmosphere, while the remaining 18% sinks to the intermediate ocean via particle scavenging. Below the mixed layer, remineralization of sinking particles releases 0.33 Mmol a^{-1} as Hg^{II}_{aq} while 0.45 Mmol a^{-1} Hg^{P}_{aq} undergoes sedimentation to the ocean floor. In subsurface water, the remineralized Hg^{II}_{aq} is reduced to Hg^{0}_{aq} and transported back to the mixed layer.

Our natural Hg simulation results in 2.7 Mmol Hg^{T} in the mixed layer (0.16 p*M* global mean concentration), 110 Mmol in the intermediate ocean (0.38 p*M*), and 840 Mmol in the deep ocean (0.82 p*M*). We find an overall lifetime of Hg in the ocean against sedimentation of 2000 years, similar to the ocean's overturning time scale. Hg^{0}_{aq} accounts for 14% of Hg^{T} in the surface ocean due to its rapid evasion to the atmosphere. This fraction increases to ~20% in the intermediate and deep oceans, because of the production of Hg^{0}_{aq} in subsurface waters from Hg^{II}_{aq}.

We found that the spatial pattern of modeled Hg^{T} concentrations in the ocean mixed layer reflects the balance between sources from the atmosphere, rivers, and upwelling of Hg-rich waters, and removal from particle sinking and evasion to the atmosphere. In the thermocline/intermediate and deep waters, we calculate strong interbasin gradients, with Hg concentrations increasing by factors of 2–3 between the North Atlantic and North Pacific Oceans. This increase with the age of water mass is the result of the continuous input of Hg from remineralization of sinking particles.

We compared the model results against observed Hg concentration profiles from 10 individual studies conducted in the Atlantic, Pacific, and Southern Oceans. The modeled Hg^{T} concentrations in the natural ocean simulation are within 50% of observations in old and deep water masses of the North Pacific Ocean, Southern Ocean, and Atlantic Ocean. The model significantly underpredicts observed Hg^{T} concentrations for younger water masses in deep water formation regions of the Southern Ocean and North Atlantic, which likely contain a strong signature from the human perturbation.

The two key uncertainties in our representation of the marine Hg cycle are (1) the value of the k_d partitioning coefficient between dissolved and particulate phases and (2) the rate of subsurface Hg^{0}_{aq} production via Hg^{II}_{aq} reduction. In addition, our simulation is sensitive to the concentration and flux of sinking particles. Better constraints on these parameters via process studies in oceanic waters and more extensive observations of speciated Hg concentration profiles in the global oceans are clearly needed. The ongoing GEOTRACES program [*Anderson et al*., 2014], with recently completed and planned cruises in the North Atlantic, South Atlantic, western Equatorial Pacific, Indian, and Arctic Oceans will be crucial in providing these constraints. Regions of particular interest for future cruises will be the South Pacific and eastern Equatorial Pacific Oceans.

Acknowledgments
We thank Steve Emerson for his helpful advice regarding the implementation of Hg chemistry in OFFTRAC and Robert P. Mason for his thoughtful comments on this manuscript.

References

Amos, H. M., et al. (2012), Gas-particle partitioning of atmospheric Hg(II) and its effect on global mercury deposition, *Atmos. Chem. Phys.*, *12*(1), 591–603.

Amos, H. M., D. J. Jacob, D. G. Streets, and E. M. Sunderland (2013), Legacy of all-time anthropogenic emissions on the global mercury cycle, *Global Biogeochem. Cycles*, *27*, 410–421, doi:10.1002/gbc.20040.

Amyot, M., G. A. Gill, and F. M. M. Morel (1997), Production and loss of dissolved gaseous mercury in coastal seawater, *Environ. Sci. Technol.*, *31*(12), 3606–3611.

Andersson, M. E., K. Gardfeldt, I. Wangberg, and D. Stromberg (2008), Determination of Henry's law constant for elemental mercury, *Chemosphere*, *73*(4), 587–592.

Anderson, R. F., E. Mawji, G. A. Cutter, C. I. Measures, and C. Jeandel (2014), GEOTRACES: Changing the way we explore ocean chemistry, *Oceanography*, *27*(1), 50–61, doi:10.5670/oceanog.2014.07.

Andren, M. O., and J. O. Nriagu (1979), The global cycle of mercury, in *Biogeochemistry of Mercury in the Environment*, edited by J. O. Nriagu, pp. 1–15, Elsevier, Amsterdam, Netherlands.

Aparicio-González, A., C. M. Duarte, and A. Tovar-Sánchez (2012), Trace metals in deep ocean waters: A review, *J. Mar. Syst.*, *100–101*, 26–33, doi:10.1016/j.jmarsys.2012.03.008.

Bagnato, E., A. Aiuppa, F. Parello, P. Allard, H. Shinohara, M. Liuzzo, and G. Giudice (2011), New clues on the contribution of Earth's volcanism to the global mercury cycle, *Bull. Volcanol.*, *73*(5), 497–510.

Bowman, K. L., T. Kading, G. J. Swarr, C. H. Lamborg, C. R. Hammerschmidt, and M. Rijkenberg (2012), Mercury species and thiols from GEOTRACES cruises in the North and South Atlantic Ocean, in Goldschmidt Conference, Montreal, Canada.

Boyd, P. W., and M. J. Ellwood (2010), The biogeochemical cycle of iron in the ocean, *Nat. Geosci.*, *3*, 675–682.

Brown, E., A. Colling, D. Park, J. Philips, D. Rothery, and J. Wright (2002), *Ocean Circulation*, edited by G. Bearmann, Butterworth-Heinemann, Oxford, U. K.

Bruland, K. W., and M. C. Lohan (2004), Controls of trace metals in seawater, in *Treatise on Geochemistry*, The Oceans and Marine Geochemistry, vol. 6, edited by H. Elderfield, pp. 23–47, Elsevier, New York.

Cohen, J. T., D. C. Bellinger, and B. A. Shaywitz (2005), A quantitative analysis of prenatal methyl mercury exposure and cognitive development, *Am. J. Prev. Med.*, *29*(4), 353–365.

Cossa, D., M.-H. Cotte-Krief, R. P. Mason, and J. Bretaudeau-Sanjuan (2004), Total mercury in the water column near the shelf edge of the European continental margin, *Mar. Chem.*, *90*, 21–29.

Cossa, D., L.-E. Heimburger, D. Lannuzel, S. R. Rintoul, E. C. V. Butler, A. R. Bowie, B. Averty, R. J. Watson, and T. Remenyi (2011), Mercury in the Southern Ocean, *Geochim. Cosmochim. Acta*, *75*, 4037–4052.

Cooke, C. A., P. H. Balcom, H. Biester, and A. P. Wolfe (2009), Over three millennia of mercury pollution in the Peruvian Andes, *Proc. Natl. Acad. Sci. U.S.A.*, *106*(22), 8830–8834.

Dai, A., and K. E. Trenberth (2002), Estimates of freshwater discharge from continents: Latitudinal and seasonal variations, *J. Hydrometeorol.*, *3*, 660–687.

Deutsch, C., S. Emerson, and L. Thompson (2005), Fingerprints of climate change in North Pacific oxygen, *Geophys. Res. Lett.*, *32*, L16604, doi:10.1029/2005GL023190.

Deutsch, C., S. Emerson, and L. Thompson (2006), Physical-biological interactions in North Pacific oxygen variability, *J. Geophys. Res.*, *111*, C09S90, doi:10.1029/2005JC003179.

Deutsch, C., H. Brix, T. Ito, H. Frenzei, and L. Thompson (2011), Climate-forced variability of ocean hypoxia, *Science*, *333*, 336, doi:10.1126/science.1202422.

Dunne, J. P., R. A. Armstrong, A. Gnanadesikan, and J. L. Sarmiento (2005), Empirical and mechanistic models for the particle export ratio, *Global Biogeochem. Cycles*, *19*, GB4026, doi:10.1029/2004GB002390.

Elbaz-Poulichet, F., L. Dezileau, R. Freydier, D. Cossa, and P. Sabatier (2011), A 3500-year record of Hg and Pb contamination in a Mediterranean sedimentary archive (the Pierre Blanche Lagoon, France), *Environ. Sci. Technol.*, *45*(20), 8642–8647.

Emerson, S. R., and J. I. Hedges (2008), *Chemical Oceanography and the Marine Carbon Cycle*, 468 pp., Cambridge Univ. Press, Cambridge, U. K, doi:10.1017/CBO9780511793202.

Fain, X., et al. (2009), Polar firn air reveals large-scale impact of anthropogenic mercury emissions during the 1970s, *Proc. Natl. Acad. Sci. U.S.A.*, *106*(38), 16,114–16,119.

Fitzgerald, W. F., D. R. Engstrom, C. H. Lamborg, C. M. Tseng, P. H. Balcom, and C. R. Hammerschmidt (2005), Modern and historic atmospheric mercury fluxes in northern Alaska: Global sources and Arctic depletion, *Environ. Sci. Technol.*, *39*, 557–568.

Fitzgerald, W. F., C. H. Lamborg, and C. R. Hammerschmidt (2007), Marine biogeochemical cycling of mercury, *Chem. Rev.*, *107*, 641–662.

Gent, P. R., and J. C. Mcwilliams (1990), Isopycnal mixing in ocean circulation models, *J. Phys. Oceanogr.*, *20*(1), 150–155.

Hallberg, R. (1995), Some aspects of the circulation in ocean basins with isopycnals intersecting the sloping boundaries, PhD thesis, Univ. of Washington, Seattle.

Hallberg, R., and P. Rhines (1996), Buoyancy-driven circulation in an ocean basin with isopycnals intersecting the sloping boundary, *J. Phys. Oceanogr.*, *26*, 913–940.

Hammerschmidt, C. R., and W. F. Fitzgerald (2004), Geochemical controls on the production and distribution of methylmercury in near-shore marine sediments, *Environ. Sci. Technol.*, *38*(5), 1487–1495, doi:10.1021/es034528q.

Hammerschmidt, C. R., and K. L. Bowman (2012), Vertical methylmercury distribution in the subtropical North Pacific Ocean, *Mar. Chem.*, *132-133*, 77–82.

Hansell, D. A., C. A. Carlson, D. J. Repeta, and R. Schlitzer (2009), Dissolved organic matter in the ocean: A controversy stimulates new insights, *Oceanography*, *22*(4), 202–211.

Holmes, C. D., D. J. Jacob, E. S. Corbitt, J. Mao, X. Yang, R. Talbot, and F. Slemr (2010), Global atmospheric model for mercury including oxidation by bromine atoms, *Atmos. Chem. Phys.*, *10*, 12,037–12,057, doi:10.5194/acp-10-12037-2010.

Kraus, E. B., and J. S. Turner (1967), A one-dimensional model of the seasonal thermocline II. The general theory and its consequences, *Tellus*, *19*, 98–106.

Lam, P. J., S. C. Doney, and J. K. B. Bishop (2011), The dynamic ocean biological pump: Insights from a global compilation of particulate organic carbon, $CaCO_3$, and opal concentration profiles from the mesopelagic, *Global Biogeochem. Cycles*, *25*, GB3009, doi:10.1029/2010GB003868.

Lamborg, C. H., W. F. Fitzgerald, J. O'Donnel, and T. Torgersen (2002), A non-steady-state compartmental model of global-scale mercury biogeochemistry with interhemispheric atmospheric gradients, *Geochim. Cosmochim. Acta*, *66*, 1105–1118.

Lamborg, C. H., K. L. Von Damm, W. F. Fitzgerald, C. R. Hammerschmidt, and R. Zierenberg (2006), Mercury and monomethylmercury in fluids from Sea Cliff submarine hydrothermal field, Gorda Ridge, *Geophys. Res. Lett.*, *33*, L17606, doi:10.1029/2006GL026321.

Lamborg, C. H., C. R. Hammerschmidt, G. A. Gill, R. P. Mason, and S. Gichuki (2012), An intercomparison of procedures for the determination of total mercury in seawater and recommendations regarding mercury speciation during GEOTRACES cruises, *Limnol. Oceanogr. Methods*, *10*, 90–100.
Laurier, F., R. Mason, G. Gill, and L. Whalin (2004), Mercury distributions in the North Pacific Ocean—20 years of observations, *Mar. Chem.*, *90*(1–4), 3–19.
Large, W. G., and S. G. Yeager (2009), The global climatology of an interannually varying air-sea flux data set, *Clim. Dyn.*, *33*(2–3), 341–364, doi:10.1007/s00382-008-0441-3.
Lehnherr, I., V. L. St. Louis, H. Hintelmann, and J. L. Kirk (2011), Methylation of inorganic mercury in polar marine waters, *Nat. Geosci.*, *4*, 298–302, doi:10.1038/NGEO1134.
Mason, R. P., and W. F. Fitzgerald (1993), The distribution and biogeochemical cycling of mercury in the equatorial Pacific Ocean, *Deep Sea Res., Part I*, *40*, 1897–1924.
Mason, R. P., W. F. Fitzgerald, and F. M. M. Morel (1994), The biogeochemical cycling of elemental mercury: Anthropogenic influences, *Geochim. Cosmochim. Acta*, *58*(15), 3191–3198.
Mason, R. P., F. M. M. Morel, and H. F. Hemond (1995), The role of microorganisms in elemental mercury formation in natural waters, *Water, Air, Soil Pollut.*, *80*, 775–787.
Mason, R., K. Rolfhus, and W. Fitzgerald (1998), Mercury in the North Atlantic, *Mar. Chem.*, *61*(1–2), 37–53.
Mason, R. P., and K. A. Sullivan (1999), The distribution and speciation of mercury in the south and equatorial Atlantic, *Deep Sea Res., Part II*, *46*, 937–956.
Mason, R. P., N. M. Lawson, and G. R. Sheu (2001), Mercury in the Atlantic Ocean: Factors controlling air-sea exchange of mercury and its distribution in the upper waters, *Deep Sea Res., Part II*, *48*, 2829–2853.
Mason, R. P. and G. R. Sheu (2002), Role of the ocean in the global mercury cycle, *Global Biogeochem. Cycles*, *16*(4), 1093, doi:10.1029/2001GB001440.
Mason, R. P., F. J. G. Laurier, L. Whalin, and G. R. Sheu (2003), The role of ocean-atmosphere exchange in the global mercury cycle, *J. Phys. IV*, *107*, 835–838.
Mason, R. P., A. L. Choi, W. F. Fitzgerald, C. R. Hammerschmidt, C. H. Lamborg, A. L. Soerensen, and E. M. Sunderland (2012), Mercury biogeochemical cycling in the ocean and policy implications, *Environ. Res.*, *119*, 101–117.
Mergler, D., H. A. Anderson, L. H. Chan, K. R. Mahaffey, M. Murray, M. Sakamoto, A. H. Stern, and Panel on Health Risks and Toxicological Effects of Methylmercury (2007), Methylmercury exposure and health effects in humans: A world concern, *Ambio*, *36*, 3–11.
Monperrus, M., A. Tessier, D. Amouroux, A. Leynaert, P. Huonnic, and O. F. X. Donard (2007), Mercury methylation, demethylation and reduction rates in coastal and marine surface waters of the Mediterranean Sea, *Mar. Chem.*, *107*, 46–63.
Morel, F. M. M., A. M. L. Kraepiel, and M. Amyot (1998), The chemical cycle and bioaccumulation of mercury, *Annu. Rev. Ecol. Syst.*, *29*, 543–566.
Najjar, R. G., and J. C. Orr (1998), Design of OCMIP-2 simulations of chlorofluorocarbons, the solubility pump and common biogeochemistry. [Available at http://www.cgd.ucar.edu/oce/OCMIP/design.pdf.]
Nightingale, P. D., G. Malin, C. S. Law, A. J. Watson, P. S. Liss, M. I. Liddicoat, J. Boutin, and R. C. Upstill-Goddard (2000), In situ evaluation of air-sea gas exchange parameterizations using novel conservative and volatile tracers, *Global Biogeochem. Cycles*, *14*, 373–387, doi:10.1029/1999GB900091.
Pirrone, N., et al. (2010), Global mercury emissions to the atmosphere from anthropogenic and natural sources, *Atmos. Chem. Phys.*, *10*, 5951–5964, doi:10.5194/acp-10-5951-2010.
Poissant, L., M. Amyot, M. Pilote, and D. Lean (2000), Mercury water-air exchange over the upper St. Lawrence River and Lake Ontario, *Environ. Sci. Technol.*, *34*, 3069–3078.
Poulain, A. J., E. Garcia, M. Amyot, P. G. Campbell, F. Raofie, and P. A. Ariya (2007), Biological and chemical redox transformations of mercury in fresh and salt waters of the high arctic during spring and summer, *Environ. Sci. Technol.*, *41*, 1883–1888.
Rolfhus, K. R., and W. F. Fitzgerald (2001), The evasion and spatial/temporal distribution of mercury species in Long Island Sound, CT-NY, *Geochim. Cosmochim. Acta*, *65*(3), 407–418.
Rolfhus, K. R., and W. F. Fitzgerald (2004), Mechanisms and temporal variability of dissolved gaseous mercury production in coastal seawater, *Mar. Chem.*, *90*(1–4), 125–136.
Schaefer, J. K., J. Yagi, J. R. Reinfelder, T. Cardona, K. M. Ellickson, S. Tel-Or, and T. Barkay (2004), Role of the bacterial organomercury lyase (MerB) in controlling methylmercury accumulation in mercury-contaminated natural waters, *Environ. Sci. Technol.*, *38*(16), 4304–4311.
Schmittner, A., J. C. H. Chiang, and S. R. Hemming (2007), Introduction: The ocean's meridional overturning circulation, in *Ocean Circulation: Mechanisms and Impacts*, *Geophys. Monogr. Ser.*, vol. 173, edited by A. Schmittner et al., pp. 1–4, AGU, Washington, D. C., doi:10.1029/173GM02.
Schuster, P. F., D. P. Krabbenhoft, D. L. Naftz, L. D. Cecil, M. L. Olson, J. F. Dewild, D. D. Susong, J. R. Green, and M. L. Abbott (2002), Atmospheric mercury deposition during the last 270 years: A glacial ice core record of natural and anthropogenic sources, *Environ. Sci. Technol.*, *36*, 2303–2310.
Selin, N. E., D. J. Jacob, R. J. Park, R. M. Yantosca, S. Strode, L. Jaegle, and D. Jaffe (2007), Chemical cycling and deposition of atmospheric mercury: Global constraints from observations, *J. Geophys. Res.*, *112*, D02308, doi:10.1029/2006JD007450.
Selin, N. E., D. J. Jacob, R. M. Yantosca, S. Strode, L. Jaeglé, and E. M. Sunderland (2008), Global 3-D land-ocean-atmosphere model for mercury: Present-day versus preindustrial cycles and anthropogenic enrichment factors for deposition, *Global Biogeochem. Cycles*, *22*, GB2011, doi:10.1029/2007GB003040.
Shao, A. E., S. Mecking, L. Thompson, and R. E. Sonnerup (2013), Mixed layer saturations of CFC-11, CFC-12, and SF_6 in a global isopycnal model, *J. Geophys. Res. Oceans*, *118*, 4978–4988, doi:10.1002/jgrc.20370.
Siddall, M., G. M. Henderson, N. R. Edwards, M. Frank, S. A. Muller, T. F. Stocker, and F. Joos (2005), ^{231}Pa/^{230}Th fractionation by ocean transport, biogenic particle flux and particle type, *Earth Planet. Sci. Lett.*, *237*, 135–155.
Siegenthaler, U., and H. Oeschger (1978), Predicting future atmospheric carbon dioxide levels, *Science*, *199*(4327), 388–395, doi:10.1126/science.199.4327.388.
Soerensen, A. L., E. M. Sunderland, C. D. Holmes, D. J. Jacob, R. M. Yantosca, H. Skov, J. H. Christensen, S. A. Strode, and R. P. Mason (2010), An improved global model for air-sea exchange of mercury: High concentrations over the north Atlantic, *Environ. Sci. Technol.*, *44*, 8574–8580, doi:10.1021/es102032g.
Soerensen, A. L., R. P. Mason, P. H. Balcom, and E. M. Sunderland (2013), Drivers of surface ocean mercury concentrations and air-sea exchange in the west Atlantic Ocean, *Environ. Sci. Technol.*, *47*, 7757–7765.
Streets, D. G., M. K. Devane, Z. Lu, T. C. Bond, E. M. Sunderland, and D. J. Jacob (2011), All-time releases of mercury to the atmosphere from human activities, *Environ. Sci. Technol.*, *45*, 10,485–91.
Strode, S., L. Jaegle, N. Selin, D. Jacob, R. Park, R. Yantosca, R. Mason, and F. Slemr (2007), Air-sea exchange in the global mercury cycle, *Global Biogeochems. Cycles*, *21*, GB1017, doi:10.1029/2006GB002766.

Strode, S., L. Jaeglé, and S. Emerson (2010), Vertical transport of anthropogenic mercury in the ocean, *Global Biogeochem. Cycles*, *24*, GB4014, doi:10.1029/2009GB003728.

Sunderland, E., and R. Mason (2007), Human impacts on open ocean mercury concentrations, *Global Biogeochem. Cycles*, *21*, GB4022, doi:10.1029/2006GB002876.

Sunderland, E. M., D. P. Krabbenhoft, J. W. Moreau, S. A. Strode, and W. M. Landing (2009), Mercury sources, distribution, and bioavailability in the North Pacific Ocean: Insights from data and models, *Global Biogeochem. Cycles*, *23*, GB2010, doi:10.1029/2008GB003425.

Trossman, D. S., L. Thompson, S. Mecking, and M. J. Warner (2012), On the formation, ventilation, and erosion of mode waters in the North Atlantic and Southern Oceans, *J. Geophys. Res.*, *117*, C09026, doi:10.1029/2012JC008090.

Whalin, L., E. Kim, and R. Mason (2007), Factors influencing the oxidation, reduction, methylation and demethylation of mercury species in coastal waters, *Mar. Chem.*, *107*, 278–294.

Wilke, C. R., and P. Chang (1955), Correlation of diffusion coefficients in dilute solutions, *AIChE J.*, *1*(2), 264–270.

Yokoo, E. M., J. G. Valente, L. Grattan, S. L. Schmidt, I. Platt, and E. K. Silbergeld (2003), Low level methylmercury exposure affects neuropsychological function in adults, *Environ. Health A Global Access Sci. Source*, *2*(8), doi:10.1186/1476-069X-2-8.